Asian Journal of Chemistry; Vol. 38, No. 7 (2026), 1912-1920
ASIAN JOURNAL OF CHEMISTRY
https://doi.org/10.14233/ajchem.2026.35861

Encapsulation of Chitosan Functionalised Zinc Oxide Nanoparticles in Nylon Nanofibre Matrix for Water-Resistant Antibacterial Coating

NAIRIKA DEKA[1], RIA GHOSH[2], LOPAMUDRA ROY[3], ASIM KUMAR MALLICK[4], SAMIR KUMAR PAL[2] and SUNANDAN BARUAH[5,*]

[1]Centre of Excellence Nanotechnology, Assam down town University, Gandhi Nagar, Panikhaiti, Guwahati-781026, India
[2]Department of Chemical and Biological Sciences, S.N. Bose National Centre for Basic Sciences, Block JD, Sector 3, Salt Lake, Kolkata-700106, India
[3]Department of Applied Optics and Photonics, JD-2, Sector-III, Salt Lake, Kolkata-700106, India
[4]Department of Pediatric Medicine, Nil Ratan Sirkar Medical College and Hospital, 38, Acharya Jagadish Chandra Bose Rd, Sealdah, Raja Bazar, Kolkata-700014, India
[5]Department of Electronics & Communication, Assam Skill University, Bidya Nagar, Gerimari, Mangaldai-784125, India

*Corresponding author: E-mail: s.baruah@asu.ac.in

Received: 6 March 2026 *Accepted*: 17 June 2026 *Published online*: 3 July 2026 AJC-22416

Entrapment of antibacterial agents in a hydrophobic self-supported environment is a challenge for their accessibility to the external environment to reach the bacterial infection. A self-supporting nylon nanofibre matrix (NNFM) embedded with chitosan-functionalised zinc oxide nanoparticles (CTS-ZnO NPs, ~50 nm) was developed as a photoactive antimicrobial nanohybrid. FTIR confirmed the successful functionalisation of ZnO NPs with chitosan, while XRD verified their crystalline wurtzite structure. DLS analysis demonstrated good colloidal stability and electron microscopy revealed the morphology and uniform distribution of the nanoparticles within the NNFM. Picosecond-resolved UV–Vis spectroscopy showed rapid transfer of photogenerated electrons from CTS-ZnO NPs to the NNFM, followed by their migration into the aqueous medium, where they generated reactive oxygen species (ROS). The combined effects of ROS production, ZnO and chitosan led to significant disruption of bacterial biofilms. The water-resistant nature of the nylon matrix further highlights the potential of this nanohybrid for smart wound dressings aimed at treating biofilm-associated bacterial infections.

Keywords: Zinc oxide, Antibacterial, Biofilm, Nanofiber, *Staphylococcus aureus*.

INTRODUCTION

A wound is a disruption of the normal structure and function of the skin caused by external injury or underlying pathological conditions [1]. Treatment of wound involves a series of tightly regulated biological events including hemostasis, inflammation, proliferation and tissue remodeling [2]. Immediately after injury, coagulation pathways are activated to control blood loss and establish a provisional matrix that supports cellular adhesion and tissue regeneration [3,4]. Successful wound management relies on dressings that protect the damaged tissue, minimise infection and promote rapid healing. The choice of dressing material is governed by its healing efficiency, affordability and ability to prevent microbial contamination [5]. Loss of skin integrity weakens the body's primary defense barrier, creating favourable conditions for microbial colonisation and infection. A moist wound environment is known to accelerate healing by supporting cell migration and tissue regeneration [6].

Synthetic polymer-based dressings have gained considerable attention since they absorb wound exudates while maintaining optimal moisture levels at the injury site. Traditional gauze dressings primarily serve as passive coverings, whereas advanced materials including foams, films, hydrocolloids and hydrogels provide effective protection against bacterial penetration [7]. Waterproof dressings offer added convenience by protecting the wound during daily activities without compromising comfort.

Natural polysaccharides have emerged as valuable alternatives in wound-care applications. Chitosan is a biodegradable

and biocompatible biomaterial recognized for its hemostatic, antimicrobial and wound-healing properties [8-10]. Its superior blood-clotting ability compared with conventional gauze makes it attractive for the treatment of hemorrhagic injuries [9]. Chitosan also stimulates polymorphonuclear leukocyte activity, promoting granulation tissue formation and wound repair [11]. Incorporation of zinc oxide nanoparticles (ZnO NPs) into chitosan matrices enhances their biological performance, producing nanocomposites with stronger antimicrobial activity, anti-inflammatory effects and improved wound closure characteristics [12,13]. ZnO NPs contribute to tissue regeneration and infection control owing to their broad-spectrum antibacterial activity, chemical stability, low toxicity and photocatalytic properties [14,15]. These attributes have established chitosan–ZnO nanocomposites as promising candidates for wound-healing and therapeutic delivery applications [16].

Considerable interest has also been directed toward chitosan nanofibers due to their high surface area, biodegradability, biocompatibility, low toxicity and antibacterial activity [17,18]. Electrospun and crosslinked chitosan nanofibers exhibit excellent wet stability, a key requirement for wound-healing materials [19]. Reports in the literature consistently demonstrate that multifunctional composite biomaterials exhibit superior performance compared with their individual constituents due to the integration of complementary structural and biological characteristics.

Based on these considerations, the present work focuses on the fabrication of a multifunctional wound-dressing platform composed of chitosan-functionalised zinc oxide nanoparticles (CTS-ZnO NPs) embedded within an electrospun nylon 66 nanofibre matrix (NNFM). Electrospinning is widely employed for the production of nonwoven fibrous scaffolds with morphological features resembling the extracellular matrix, making them attractive for biomedical applications [20]. Nylon 66 was selected as the supporting matrix due to its biocompatibility, mechanical durability and water-resistant nature [21]. Electrospun nylon 66 nanofibers have demonstrated significant potential in tissue engineering and wound-healing applications [22-24]. On the other hand, ZnO NPs are familiar with their antibacterial activity, non-toxicity, high stability and excellent photocatalytic capabilities [25]. Thus, embedding of CTS-ZnO NPs into the nylon matrix enhances the antimicrobial and photocatalytic performance of the composite while improving its structural stability through the combined effects of chitosan and ZnO within the nylon framework.

Therefore, the objective of this study was to synthesize and characterize CTS-ZnO NP-loaded NNFM and examine its suitability as an antimicrobial wound dressing with potential utility against biofilm-associated hospital-acquired infections. UV-visible spectroscopy was employed to characterize the nano-hybrid matrix. Successful functionalisation of ZnO NPs with chitosan was verified through fluorescence spectroscopy and time-correlated single-photon counting (TCSPC) analysis. These investigations revealed suppression of oxygen vacancy related defects and improved aqueous stability of the nanoparticles after chitosan coating. Biocompatibility of the developed matrix was evaluated through hemolysis assays. Light-induced reactive oxygen species (ROS) generation was examined and correlated with antibacterial activity against *S. aureus*.

EXPERIMENTAL

Zinc oxide nanopowder, chitosan, nylon, acetic acid and formic acid were purchased from Sigma-Aldrich, USA. The solvent ethanol was procured from Merck Ltd., India and 2,7-dichlorodihydrofluorescein diacetate (DCFH-DA) was bought from Calbiochem to estimate the reactive oxygen species (ROS) production. Nanopore water, with a resistivity value ≥ 18 MΩ cm, from the Milli-Q system (Millipore GmbH, Germany) was used in all experimentsFor bacterial studies, Luria–Bertani (LB) broth and LB top agar were procured from HIMEDIA, India. The Gram-positive bacteria, *S. aureus* strain 1692, was procured from ATCC.

Chitosan functionalised zinc oxide nanoparticles (CTS-ZnO NPs) synthesis: In 10 mL of acetic acid, 110 mg of low-molecular weight chitosan was dissolved under vigorous stirring. The solution was kept at room temperature overnight while stirring. Then 20 mg of ZnO nanopowder were added to the solution for the preparation of CTS-ZnO NPs.

Preparation of electrospun NNFM: In 20 mL of formic acid 2 g of nylon were added under mild stirring at room temperature [26]. After the nylon got dissolved, the prepared chitosan-capped nanoparticles were added dropwise (2 mL). The prepared sample was introduced into a syringe with a nozzle diameter of 2 mm. The distance between the nozzle and the nanofiber collection plate was 17 cm. The power supplied to generate nanofibers was 18 KV with a flow rate of 6 μL. A shower of nanofiber samples confirmed the formation of nanofibers. After 45 min, the collection of NNFM was peeled from the substrate [27].

Preparation of biofilm: A small quantity of *S. aureus* bacterial culture was introduced into LB broth (5 mL), a medium suitable for the growth of *S. aureus* biofilm. The bacterial culture was spread onto polycarbonate Petri dishes and placed in an incubator set at 37 ºC for 2 days. To measure the amount of biofilm formed, the attached cells were washed and the unattached cells were removed. The coverslips were then washed with water and stained with 0.1% CV solution. After 30 min, the CV solution was removed and the remaining stain was dissolved in 95% ethanol. The absorbance peak at 595 nm was measured of the dissolved stain, which indicates the extent of bacterial adherence and biofilm formation on the coverslip surface [28]. To study the morphological changes in the biofilms under different treatment conditions, 200 μL of the bacterial broth was placed on coverslips and incubated for 24 h at 37 ºC. The samples were then washed with water, fixed with 2.5% glutaraldehyde, dehydrated with alcohol and air-dried. FESEM was used for qualitative assessment of the appearance of the biofilms. The coverslips were coated with gold and examined using a field emission scanning electron microscope (Quanta FEG 250). When the microscope operated at an accelerating voltage of 200 V to 30 kV and under low vacuum conditions at 30 kV, the resolution was 5.0 nm. The image was captured using a large field secondary electron detector for low vacuum operation.

Characterisation: Optical absorbance spectra of samples were measured in a double-beam UV-vis spectrophotometer (model UV-2600, Shimadzu, Japan) in the 200-800 nm wavelength range. The room temperature steady-state emission

spectra were recorded using a Fluorolog Model LFI-3751 (Horiba-Jobin Yvon, Edison, USA) spectrofluorometer equipped with a microchannel plate–photomultiplier tube (MCP-PMT, Hamamatsu, Japan). A JASCO FTIR-6300 spectrometer apparatus (Oklahoma City, OK, USA) was used to perform Fourier transform infrared spectroscopy (FTIR) on the liquid samples. For the measurements of dynamic light scattering (DLS) and ζ potential, a NanoS Malvern (Zeta-sizer) apparatus with a 4 mWHe:Ne laser (λ = 632.8 nm) and a thermostat connected sample chamber was used. Empyrean powder X-ray diffractometer was used for analyzing the crystallinity of ZnO nanopowder solid samples was prepared in the form of dry powder of 300 mesh about 3 g of sample on glass slide of size 2 cm × 3.5 cm and thickness 0.2 cm with uniform layer of size 2 cm × 1.5 cm on one side. All the PL transients were measured using the picosecond-resolved time-correlated single photon counting (TCSPC) technique. A picosecond diode laser pumped (LifeSpec-ps) fluorescence spectrophotometer from Edinburgh Instruments, U.K. Picosecond excitation pulses from the piquant diode laser was used at 375 nm with an instrument response function (IRF) of 60 ps. To detect the PL from the sample after dispersion through a monochromator a microchannel-plate photomultiplier tube (MCP-PMT, Hamamatsu, Japan) was used. For all transients, the polarizer on the emission side was adjusted to be at 55º concerning the polarisation axis of the excitation beam. Native and BR-capped UV irradiated human serum albumin (HSA) structures were characterised by circular dichroism (CD) measurements in a JASCO 815 spectro-polarimeter at 20 ± 0.1 ºC. The scan speed of the measurements was 100 nm min^{-1} and each spectrum was the average of five scans. The spectral data were acquired over the range of 330-220 nm using a 2 mm path length cuvette. All fluorescence spectra were corrected for variations with a wavelength in source intensity, photomultiplier response and monochromator throughput. The structural morphologies and chemical compositions of the synthesised chitosan-capped ZnO NPs from different sources were analysed using FESEM and EDAX methods. Before scanning in a FESEM (Quanta FEG 250), the coverslips containing samples were coated with gold. For the measurement of water contact angle custom designed contact angle measurement instrument was used.

Quantification of ROS: ROS generation was quantified using 2,7-dichlorofluorescein (DCFH), a well-established fluorescent probe. DCFH was prepared through de-esterification of DCFH-DA at room temperature, following a standardised protocol as reported in the literature. Upon exposure to light, ROS generated by the NNFM oxidised DCFH to its fluorescent derivative, dichlorofluorescein (DCF), which exhibits a characteristic emission maximum at 520 nm when excited at 488 nm. DCF emission spectra were recorded using a Fluorolog Model LFI-3751 spectrofluorometer (Horiba-Jobin Yvon, Edison, USA). All ROS quantification experiments were conducted under light irradiation for a duration of 15 min.

Hemolysis assay: Cytotoxicity of the NNFM was evaluated through a hemolysis assay using human red blood cells (RBCs), conducted under approved ethical clearance no. (No/NMC/443). Human blood was collected in heparinised tubes and divided into three experimental groups: a PBS control, a negative control, and an NNFM-treated group. The negative control consisted of RBCs incubated in water to induce 100% hemolysis as a reference, while the NNFM-treated group involved direct exposure of RBCs to the prepared matrix. All three groups were incubated for 30 min, followed by centrifugation at 1200 rpm for 4 min. The degree of hemolysis was subsequently determined by measuring the absorbance of the resulting supernatant.

Statistical analysis: Mean ± standard deviation (SD) was used to express quantitative data unless otherwise specified. Statistical analyses were performed using GraphPad Prism software (version 5.00 for Windows; GraphPad Software, California, USA). Differences between groups were considered statistically significant at $p < 0.05$.

RESULTS AND DISCUSSION

Morphological studies: TEM analysis of the synthesised CTS-ZnO NPs (Fig. 1) revealed a spherical morphology with an average diameter of 60.03 ± 0.23 nm (Fig. 1 inset). The

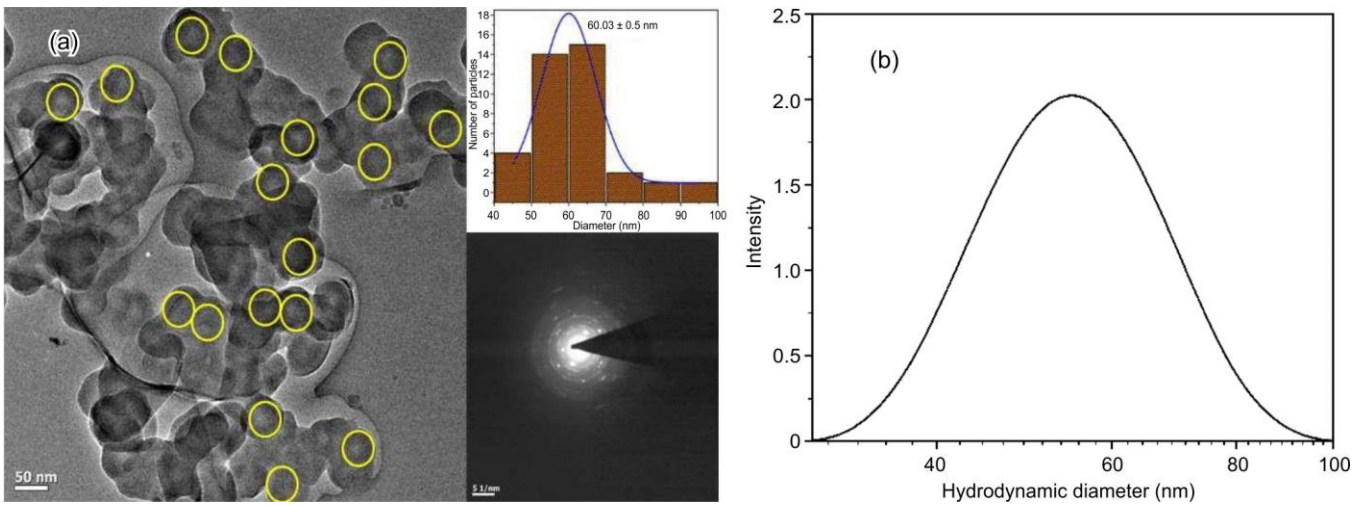

Fig. 1. (a) TEM micrographs of the as-prepared CTS- ZnO NPs. Inset: SAED pattern revealing the crystalline nature of the CTS- ZnO NPs. Size distribution of CTS- ZnO NPs. (b) Hydrodynamic diameter of the ZnO NPs after its functionalisation with chitosan

crystalline nature of the nanoparticles was further confirmed by selected area electron diffraction (SAED) pattern (Fig. 1 inset). Dynamic light scattering (DLS) measurements resulted a hydrodynamic diameter of 54.57 ± 7.9 nm, a polydispersity index (PDI) of 0.4, and a zeta potential of +39.5 ± 7.35 mV. The positive zeta potential confirms successful capping of ZnO NPs with chitosan, indicating stable electrostatic stabilisation of the nanoparticles in suspension.

Following synthesis and characterisation of CTS-ZnO NPs, electrospinning was employed to fabricate both the nylon nanofiber matrix (NFM) and the CTS-ZnO NP-incorporated nylon nanofiber matrix (NNFM). TEM micrographs revealed nanofibers with an average diameter of approximately 63 nm for the NFM (Fig. 2a), while the NNFM exhibited a slightly larger diameter of ~66 nm along with higher contrast (Fig. 2b), consistent with the successful incorporation of CTS-ZnO NPs within the nylon matrix. The marginal increase in fiber diameter further corroborates the embedding of nanoparticles into the fibrous structure.

Elemental composition of both NFM and NNFM was analysed through energy dispersive spectroscopy (EDS), with the corresponding patterns and atomic percentages of constituent elements presented in Fig. 3, providing additional confirmation of CTS-ZnO NP integration within the nanofiber matrix.

XRD studies: The crystalline structure of the synthesised ZnO NPs was further investigated by powder X-ray diffraction (XRD), as shown in Fig. 4. The XRD pattern exhibited sharp and intense diffraction peaks, indicative of high crystallinity. Diffraction peaks observed at 2θ values of approximately 31.7º, 34.4º, 36.2º, 47.5º, 56.6º, 62.8º, 66.3º, 67.9º and 69.1º were indexed to the (100), (002), (101), (102), (110), (103), (200), (112), and (201) crystal planes, respectively, consistent with the hexagonal wurtzite phase of ZnO (JCPDS card No. 36-1451, PDF No. 01-089-0510), thereby confirming the phase purity and crystalline integrity of the synthesised nanoparticles.

FT-IR studies: FTIR spectroscopy was performed on ZnO NPs, chitosan (CTS) and CTS-ZnO NPs to confirm the efficient capping of ZnO NPs with CTS and to investigate the consequential spectral changes in the nanocomposite (Fig. 5). In the FTIR spectrum of ZnO NPs, characteristic peaks at 2975, 2923, 2883, 1322, 1089 and 1049 cm^{-1}, attributable to

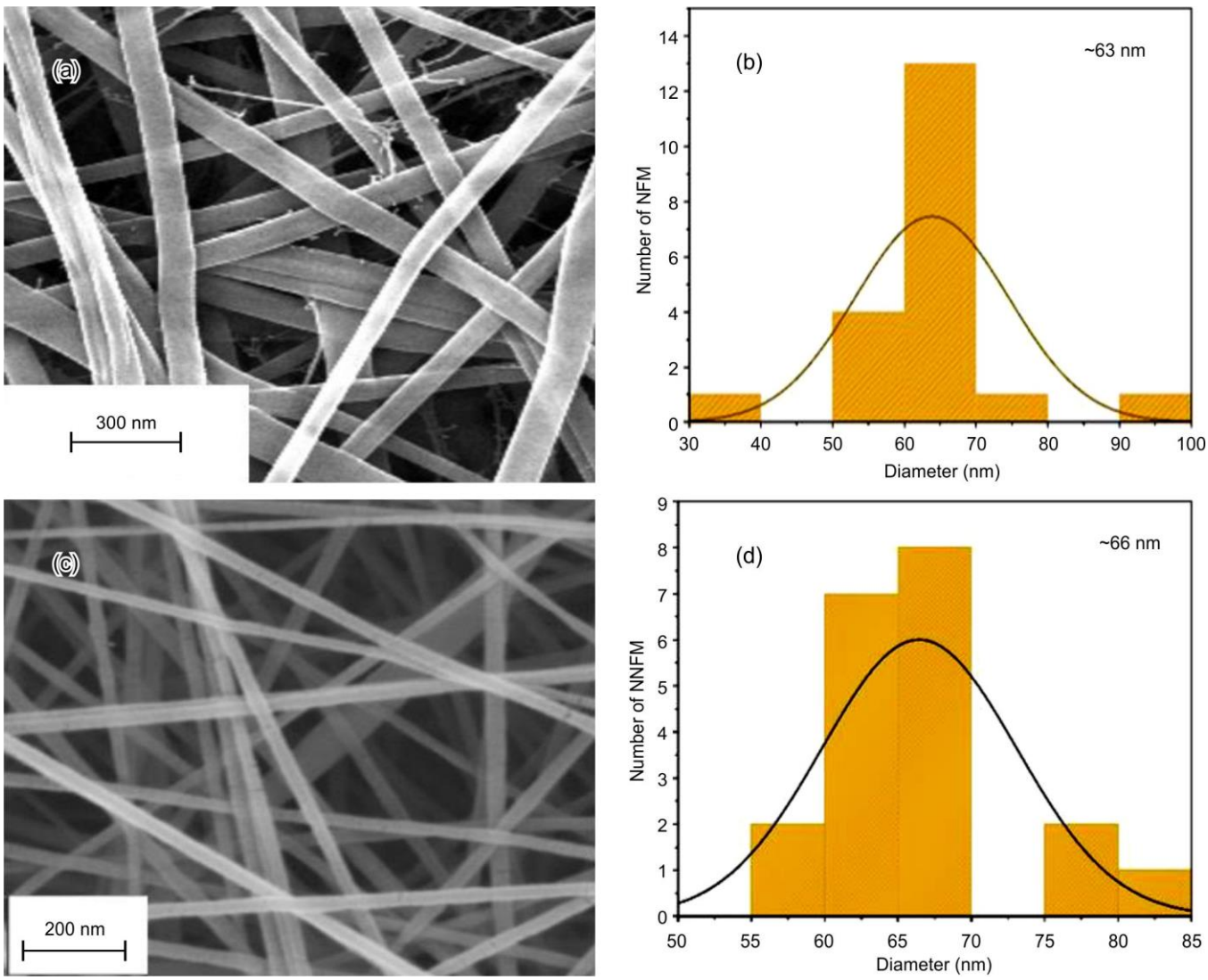

Fig. 2. FESEM images of (a) NFM with diameter of ~63 nm and (c) NNFM with diameter of ~66 nm

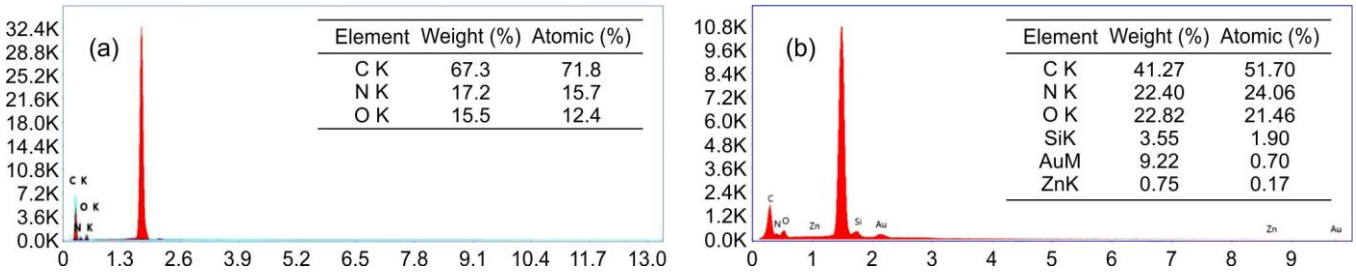

Fig. 3. EDS patterns of NFM (a) and NNFM (b) with atomic percentage of the elements

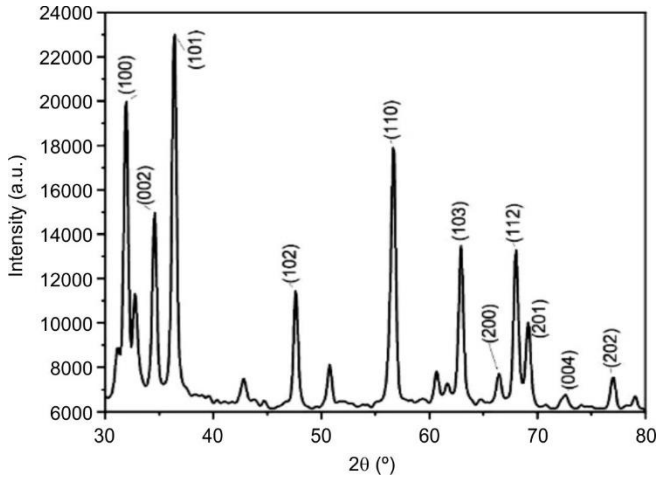

Fig. 4. XRD pattern of ZnO NPs indicating high crystalline in nature

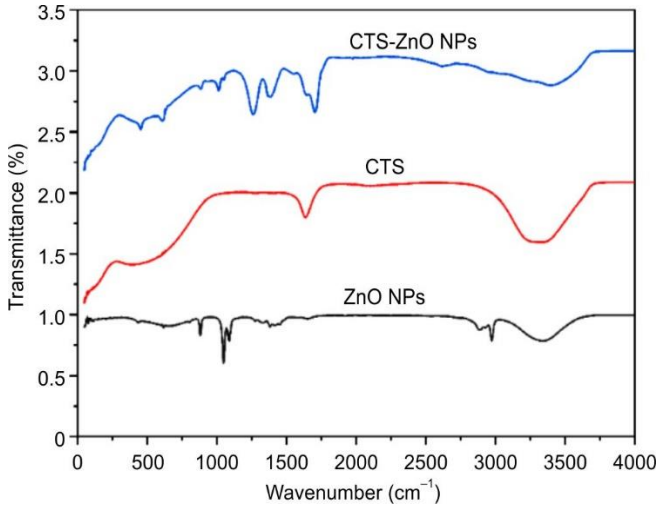

Fig. 5. FTIR spectra of ZnO NPs, CTS and CTS-ZnO NPs

the carbonyl-linked fragments of zinc acetate dihydrate on the ZnO surface, were also observed in the CTS-ZnO NPs spectrum with slight shifts, indicating surface interaction between the two components. Furthermore, the signature NH bending vibration of the primary amino (-NH_2) group of CTS, appearing at 1639 cm^{-1}, was shifted to 1650 cm^{-1} in the CTS-ZnO NPs spectrum, confirming effective chemical interaction between chitosan and the ZnO NP surface. Hence, the observed spectral shifts confirm the successful surface capping of ZnO NPs with CTS.

Optical studies: Fig. 6 depicts the UV-vis absorbance spectrum of the chitosan-capped zinc oxide nanoparticles

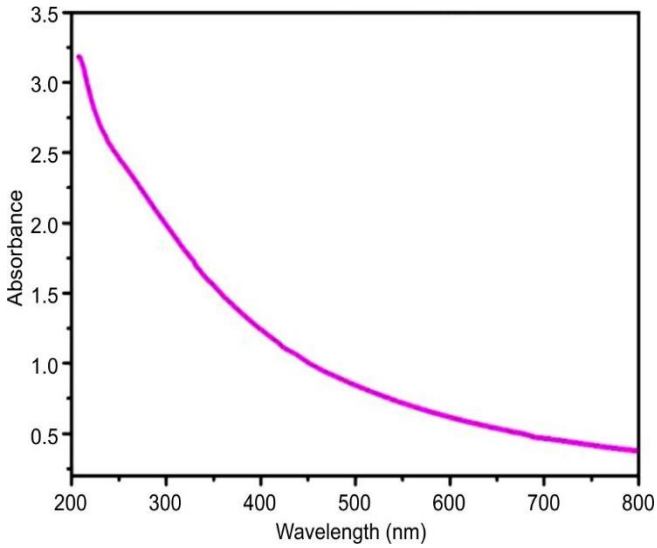

Fig. 6. Differential UV-vis absorbance spectra of NNFM in ethanol

(CTS-ZnO NPs) embedded nylon matrix (CTS-ZnO NNFM). An absorbance peak near 290 nm showed the evidence of nylon material whereas a broad absorbance band extending from 300 nm to 360 nm showed the footprint of CTS-ZnO NPs inside the nylon matrix.

Steady-state fluorescence emission spectra of the NNFM in Fig. 7a clearly show the NNFM contains CTS-ZnO NPs within it as a strong emission band near 430 nm appears after exiting the matrix with a 350 nm light beam. This emission comes from the defect state (oxygen vacancy centre, V_o^x). It is well known that ZnO has two oxygen defect states, one is near the surface layer (oxygen vacancy centre, V_o^{++}) of the ZnO NPs and the other far from the surface layer (V_o^x) of ZnO NPs. Due to the passivation of ZnO NPs surface, the recombination of electrons from the conduction band with a deep electron trapping centre V_o^{++}, which gives 550 nm emission becomes less favourable and the energy transfers from the defect state present in the bulk of ZnO NPs (*i.e.* near 430 nm). The emission of CTS-ZnO NPs from the NNFM sample is confirmed by the excitation spectrum of the NNFM sample depicted in Fig. 7b. It provides the signature absorbance peaks of nylon matrix at about 290 nm and ZnO NPs at ~360 nm. These findings confirm the successful fabrication of the nanofibre matrix with CTS-ZnO NPs effectively incorporated into its structure.

Ultrafast dynamics study: Picosecond-resolved fluorescence transient measurements were carried out on the CTS-ZnO NNFM and the pristine nylon matrix to examine the

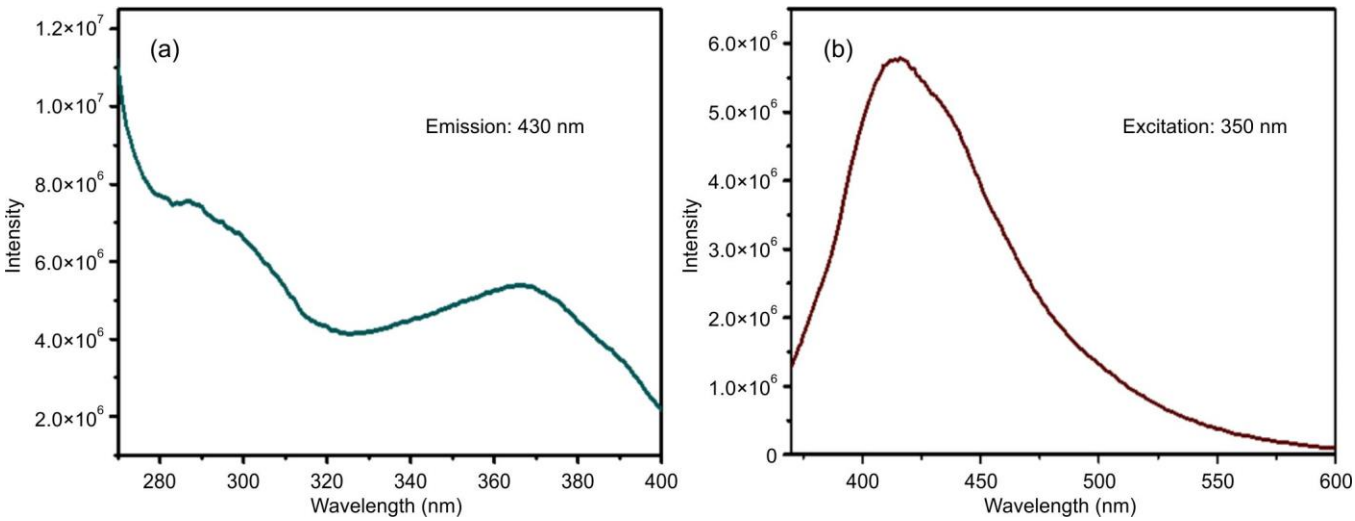

Fig. 7. (a) Emission spectra of CTS-ZnO functionalised nano fibre matrix (NNFM) and (b) Excitation spectra of CTS-ZnO functionalised nano fibre matrix (NNFM)

influence of CTS-ZnO NPs on the excited-state relaxation dynamics (Fig. 8). Fluorescence decay profiles were recorded at emission wavelengths of 430 and 550 nm (Fig. 8a-b), corresponding to defect-related and matrix-associated emission regions, respectively. At 430 nm, the CTS-ZnO NNFM exhibited a distinctly faster decay than the bare nylon matrix. The reduction in fluorescence lifetime is attributed to efficient electron transfer from defect states within the ZnO NPs to the surrounding matrix through the chitosan interface. This accelerated deactivation pathway reflects strong electronic coupling between CTS-ZnO NPs and the nylon nanofibre network. The presence of a shorter lifetime component at this wavelength is associated with the recombination of electrons trapped at oxygen-vacancy defect centres (VOx) with the valence band, followed by rapid transfer of the released energy to the surrounding system.

In contrast, the decay profiles recorded at 550 nm showed only minor variations between the CTS-ZnO NNFM and the pristine nylon matrix confirmed that the excited-state processes contributing to emission in this spectral region are less affected by the incorporation of CTS-ZnO NPs. The wavelength dependent decay behaviour demonstrates that the charge transfer process is predominantly governed by defect-mediated electronic states of ZnO. The fluorescence transient parameters summarized in Table-1 support these observations. The shorter average lifetime observed at 430 nm provides clear evidence for the successful encapsulation of ZnO NPs by chitosan and their effective integration within the nylon nanofibre matrix.

Water contact angle measurement: The water contact angle of the NNFM was measured at 135°, confirming its hydrophobic and water-resistant nature (Fig. 9), which is advantageous for wound dressing applications.

ROS generation and biocompatibility study: The ROS generation capability of the CTS-ZnO NNFM was investigated using the DCFH assay, and the results are presented in Fig. 10. As shown in Fig. 10a, the CTS-ZnO NNFM produced a significantly higher ROS signal under UV irradiation than the control samples. This enhanced ROS production originates from the photoexcitation of ZnO nanoparticles embedded within

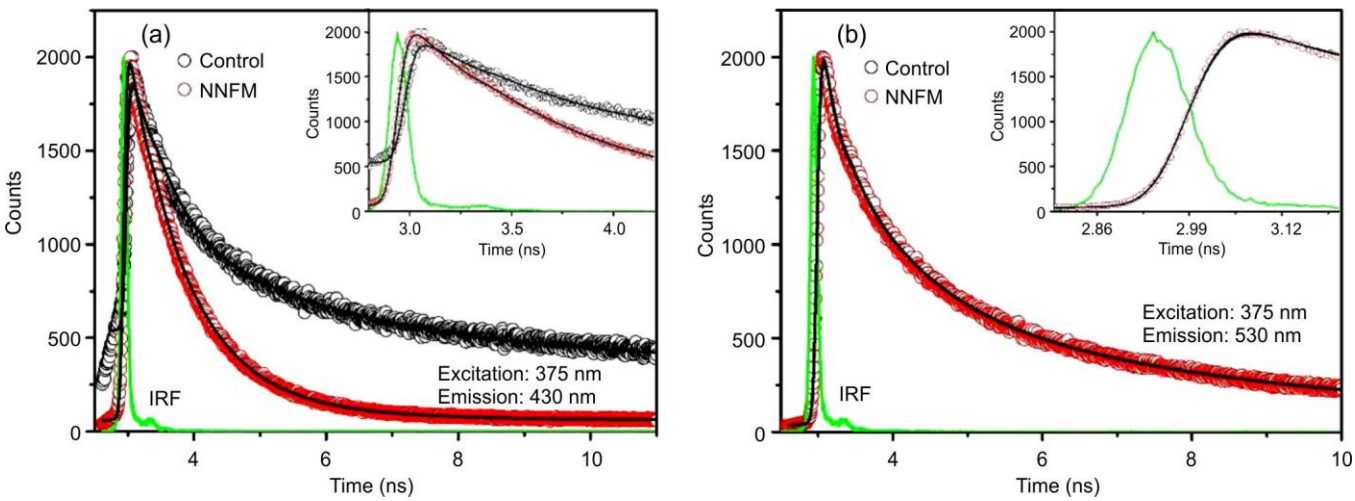

Fig. 8. Fluorescence transients of CTS-ZnO functionalised nano fibre matrix and control polymer matrix at (a) 430 nm and (b) 530 nm

TABLE-1
FLUORESCENCE TRANSIENT PARAMETERS

System	τ1 (ns)	τ2 (ns)	τ3 (ns)	τavg (ns)
NNFM (430 nm)	0.2251 ± 0.011255 (20%)	0.8681 ± 0.043405 (80%)	–	0.7395 ± 0.036975
Nanofiber (430 nm)	0.5392 ± 0.02696 (8%)	6.044 ± 0.3022 (92%)	–	5.604 ± 2802
NNFM (530 nm)	0.200 ± 0.01 (40%)	1.120 ± 0.056 (40%)	5.412 ± 0.2706 (20%)	1.610 ± 0.0805
Nanofiber (530 nm)	0.1632 ± 0.00816 (40%)	1.000 ± 0.05 (40%)	5.132 ± 0.2566 (20%)	1.492 ± 0.0746

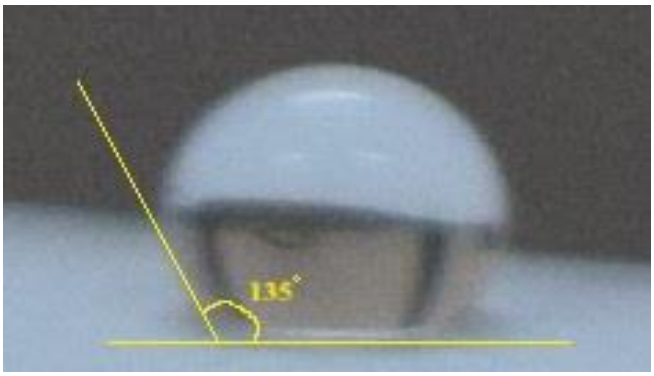

Fig. 9. Water contact angle (135°) of NNFM

the nanofibre matrix, followed by the migration of photo-generated charge carriers to the surrounding medium, where they participate in ROS formation.

The biocompatibility of the CTS-ZnO NNFM was evaluated through a hemolysis assay using human red blood cells (RBCs). The fabricated matrix induced only 1.3% hemolysis (Fig. 10b), a value well below the acceptable threshold for hemocompatible biomaterials. Microscopic examination of RBCs after exposure to the matrix revealed no detectable alterations in cell morphology compared with the control group (Fig. 10c). The retention of normal cellular morphology, together with the low hemolysis percentage, demonstrates that the CTS-ZnO NNFM exerts minimal adverse effects on RBC membranes. These findings establish the excellent hemocompatibility and biocompatibility of the developed nanohybrid matrix, supporting its potential use as a safe and effective wound-dressing material.

Antibacterial study: The antibacterial activity of the CTS-ZnO NNFM was evaluated against *S. aureus* biofilms. Optical microscopy and FESEM images (Fig. 11) revealed substantial disruption of the established biofilm following treatment with the nanohybrid matrix. Approximately 70% biofilm inhibition was achieved, demonstrating strong antibiofilm efficacy. Coupled with its excellent hemocompatibility, the CTS-ZnO NNFM shows considerable potential as a water-resistant antibacterial wound dressing for preventing bacterial colonization and biofilm-associated wound infections.

Conclusion

In this study, a novel self-supporting nylon nanofiber matrix (NNFM) was developed incorporating chitosan-functionalised zinc oxide nanoparticles. The structural charact-

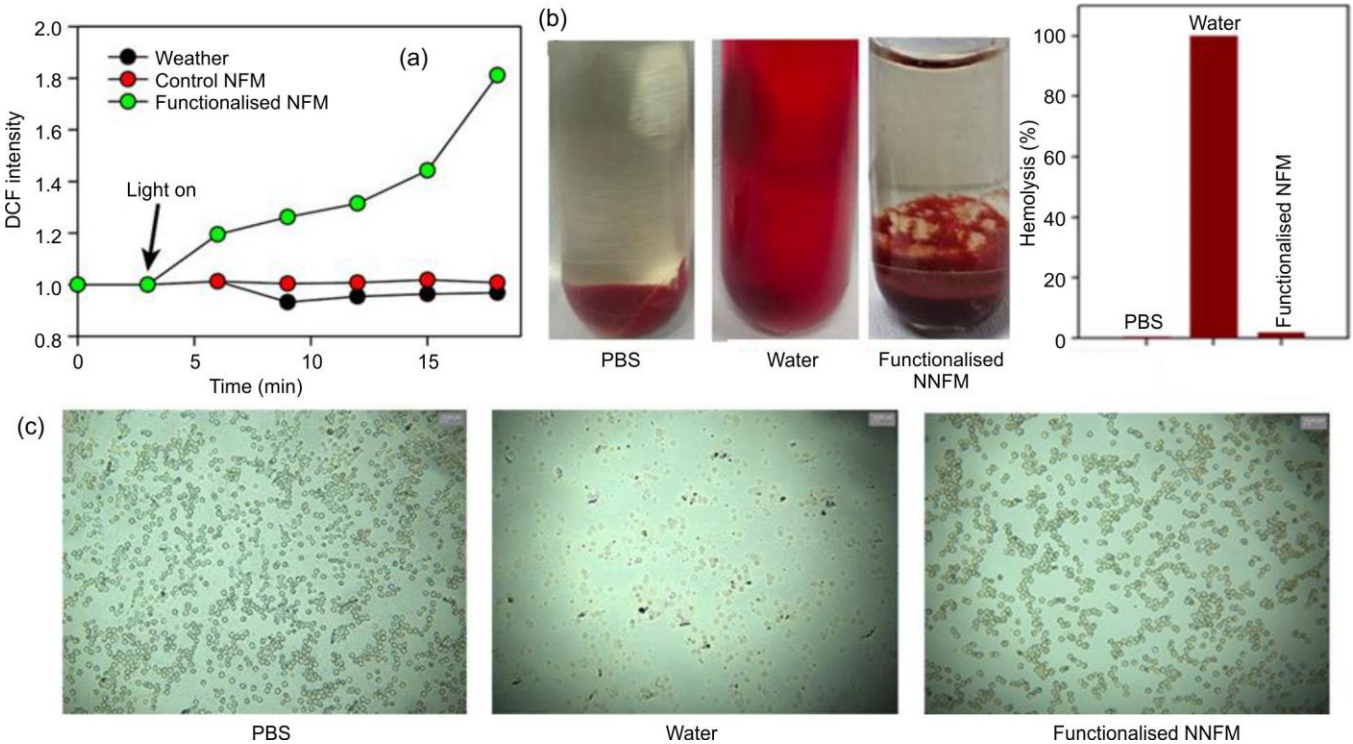

Fig. 10. (a) ROS generation activity of the CTS-ZnO functionalised nano fibre matrix on UV light irradiation, (b) hemolysis assay of CTS-ZnO functionalised nano fibre matrix (NNFM) and (c) microscopic images showing the morphology of RBCs

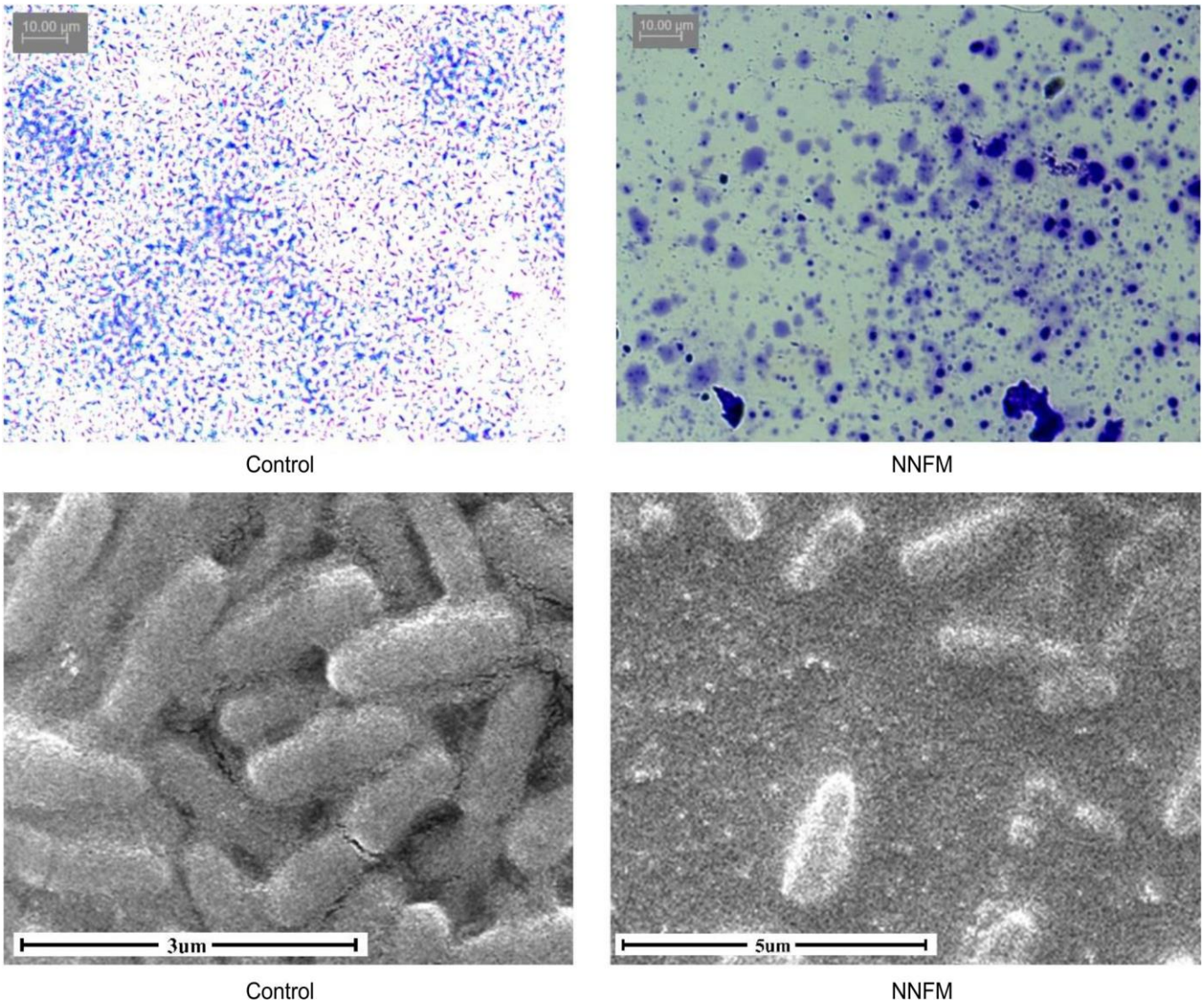

Fig. 11. Optical and FESEM images of *S. aureus* biofilm for (a) and (b) control (c) and (d) CTS-ZnO functionalised nano fibre matrix (NNFM)

erisation and ultrafast dynamics of photogenerated electrons transferring from the ZnO nanohybrid to the host NNFM were investigated through detailed electron microscopy and pico-second-resolved UV-Vis spectroscopy. Entrapment of anti-bacterial agents within the hydrophobic self-supported matrix facilitated reactive oxygen species (ROS) generation, which resulted in significant disruption of staphylococcal biofilm, thereby impeding bacterial infection propagation. These find-ings confirm the potential of the novel CTS-ZnO NNFM as an effective water-resistant bandage for the treatment of bacteria-infected wounds.

ACKNOWLEDGEMENTS

The authors would like to acknowledge Assam down town University for financial support to SB for procurement of instrument under ref no. AdtU/R/2022/164 and Indian National Academy of Engineering for awarding the Abdul Kalam Technology Innovation National Fellowship to SKP, INAE/ 121/AKF. The authors are also grateful to Mr. Devabrata Sarmah, Dr. Amrita Banerjee and Dr. Arpita Chattopadhyay for their help and suggestions for the design of the experiments for the work.

CONFLICT OF INTEREST

The authors declare that there is no conflict of interests regarding the publication of this article.

DECLARATION OF AI-ASSISTED TECHNOLOGIES

During the preparation of this manuscript, the authors used an AI-assisted tool(s) to improve the language. The authors reviewed and edited the content and take full responsibility for the published work.

REFERENCES

1. N.J. Percival, *Surgery*, **20**, 114 (2002); https://doi.org/10.1383/SURG.20.5.114.14626
2. T. Velnar, T. Bailey and V. Smrkolj, *J. Int. Med. Res*., **37**, 1528 (2009); https://doi.org/10.1177/147323000903700531

3. W.T. Lawrence, *Clin. Plast. Surg*., **25**, 321 (1998); https://doi.org/10.1016/S0094-1298(20)32467-6
4. M. Mir, M. N. Ali, A. Barakullah, A. Gulzar, M. Arshad, S. Fatima and M. Asad, *Prog. Biomater*., **7**, 1 (2018); https://doi.org/10.1007/s40204-018-0083-4
5. T. Helfman, L. Ovington and V. Falanga, *Clin. Dermatol*., **12**, 121 (1994); https://doi.org/10.1016/0738-081X(94)90262-3
6. G.D. Winter, *Nature*, **193**, 293 (1962); https://doi.org/10.1038/193293a0
7. S. Dhivya, V.V. Padma and E. Santhini, *BioMedicine*, **5**, 22 (2015); https://doi.org/10.7603/s40681-015-0022-9
8. M. Yadav, B. Kaushik, G. K. Rao, C. M. Srivastava and D. Vaya, *Carbohydr. Polym. Technol. Appl*., **5**, 100323 (2023); https://doi.org/10.1016/j.carpta.2023.100323
9. S.B. Gustafson, P. Fulkerson, R. Bildfell, L. Aguilera and T.M. Hazzard, *Prehosp. Emerg. Care*, **11**, 172 (2007); https://doi.org/10.1080/10903120701205893
10. T. Dai, M. Tanaka, Y.Y. Huang and M.R. Hamblin, *Expert Rev. Anti Infect. Ther*., **9**, 857 (2011); https://doi.org/10.1586/eri.11.59
11. H. Ueno, T. Mori and T. Fujinaga, *Adv. Drug Deliv. Rev*., **52**, 105 (2001); https://doi.org/10.1016/S0169-409X(01)00189-2
12. G. Shu, D. Xu, S. Xie, L.-J. Chang, X. Liu, J. Yang, Y. Li and X. Wang, *Appl. Surf. Sci*., **611**, 155727 (2023); https://doi.org/10.1016/j.apsusc.2022.155727
13. L.B. Rice, *Am. J. Infect. Control*, **34**, S11 (2006); https://doi.org/10.1016/j.ajic.2006.05.220
14. T.A. Singh, A. Sharma, N. Tejwan, N. Ghosh, J. Das and P.C. Sil, *Adv. Colloid Interface Sci*., **295**, 102495 (2021); https://doi.org/10.1016/j.cis.2021.102495
15. M. Laurenti and V. Cauda, *Nanomaterials*, **7**, 374 (2017); https://doi.org/10.3390/nano7110374
16. P. Pino, F. Bosco, C. Mollea and B. Onida, *Pharmaceutics*, **15**, 970 (2023); https://doi.org/10.3390/pharmaceutics15030970
17. A.M. Abdelgawad, S.M. Hudson and O.J. Rojas, *Carbohydr. Polym*., **100**, 166 (2014); https://doi.org/10.1016/j.carbpol.2012.12.043
18. L.M. Amirabad, M. Jonoobi, N.S. Mousavi, K. Oksman, A. Kaboorani and H. Yousefi, *Carbohydr. Polym*., **189**, 229 (2018); https://doi.org/10.1016/j.carbpol.2018.02.041
19. C. Cui, S. Sun, S. Wu, S. Chen, J. Ma and F. Zhou, *Eng. Regen*., **2**, 82 (2021); https://doi.org/10.1016/j.engreg.2021.08.001
20. A.L.G. Millas, R. McKean, R. Stevens, M. Yusuf, J.V.W. Silveira, M.B. Puzzi and E. Bittencourt, *J. Biomater. Tissue Eng*., **4**, 217 (2014); https://doi.org/10.1166/jbt.2014.1162
21. M. Shakiba, E.R. Ghomi, F. Khosravi, S. Jouybar, A. Bigham, M. Zare, M. Abdouss, R. Moaref and S. Ramakrishna, *Polym. Adv. Technol*., **32**, 3 368 (2021); https://doi.org/10.1002/pat.5372
22. J.S. Stephens, D.B. Chase and J.F. Rabolt, *Macromolecules*, **37**, 877 (2004); https://doi.org/10.1021/ma0351569
23. R. Nirmala, J.W. Jeong, H.J. Oh, R. Navamathavan, M. El-Newehy, S.S. Al-Deyab and H.Y. Kim, *Fibers Polym*., **12**, 1021 (2011); https://doi.org/10.1007/s12221-011-1021-4
24. A. Allafchian, S. A. H. Jalali and N. Kabirzadeh, *Micro Nano Lett*., **13**, 1747 (2018); https://doi.org/10.1049/mnl.2018.5142
25. M.K. Saba and R. Amini, *Food Chem*., **232**, 721 (2017); https://doi.org/10.1016/j.foodchem.2017.04.076
26. Y.H. Nien, C.N. Chang, P.L. Chuang, C.H. Hsu, J.L. Liao and C.K. Lee, *Polymers*, **13**, 1984 (2021); https://doi.org/10.3390/polym13121984
27. J. Xue, T. Wu, Y. Dai and Y. Xia, *Chem. Rev*., **119**, 5298 (2019); https://doi.org/10.1021/acs.chemrev.8b00593
28. D. Bagchi, V S.S. Rathnam, P. Lemmens, I. Banerjee and S.K. Pal, *ACS Omega*, **3**, 10877 (2018); https://doi.org/10.1021/acsomega.8b00716